Available online at www.sciencedirect.com
ScienceDirect
Progress in Natural Science 19 (2009) 1109–1117
Progress in Natural Science
www.elsevier.com/locate/pnsc

Constrained oscillation of a bubble subjected to shock wave in microvessel

Farong Gao, Caihua Xiong *, Youlun Xiong

Institute of Rehabilitation and Medical Robotics, State Key Lab of Digital Manufacturing Equipment and Technology, School of Mechanical Science and Engineering, Huazhong University of Science and Technology, Wuhan 430074, China

Received 8 September 2008; received in revised form 26 September 2008; accepted 7 October 2008

Abstract

A three-phase coupled model of the gas–liquid–solid oscillation system is established to analyze the oscillation characteristics of a bubble inside a micro blood vessel with various radii and its shape changes with different interface boundaries. The results show that unlike the spherical symmetric oscillation in an unbounded fluid, the oscillating bubble has significant asymmetric characteristics under the constraint of a flexible microvessel, especially while its radius reduces to the same order of magnitude as that of the bubble. Moreover, the variation of microbubble motion, whether the geometric shape or oscillation feature, exhibits obvious differences in the micro blood vessel compared with the rigid wall. The reasons behind these phenomena are analyzed in this paper. The conclusions have significant importance in the understanding of the mechanism of microvessel injury in ultrasound therapy.

Keywords: Asymmetric oscillation; Microbubble; Shock wave; Micro blood vessel; Boundary effects

1. Introduction

Ultrasound contrast agents have gradually been used in medical diagnosis and clinical therapy with the development of biomedical and pharmaceutical techniques [1,2]. These agents are bubble-like encapsulated micro thin shells, filled with gas, ranging from several microns in diameter, which are constructed of various biological materials such as lipid, protein, and polymer [3]. After being injected into the bloodstream, ultrasound contrast agents may enhance the ultrasonic scattering signals with their intrinsic resonance scattering properties and can easily distinguish the capillary and small blood vessel from surrounding tissues, so as to acquire high contrast ultrasonic images [4,5]. Recent research shows that the structural features of the contrast agents are well fit for the carriers of drug delivery in the microvascular system, since the drug can be effectively transported by the agents with its function of encapsulation or sorption. When microbubbles circulate in the bloodstream and arrive at the local lesion site, a high intensive ultrasound pulse (shock wave) is exerted on the bubble surface to impel the drug release, which is especially of use for tumor and gene therapy [6,7].

In ultrasonic therapy, oscillation and rupture of the microbubble induced by the shock wave have been indicated as one of the primary mechanisms for vascular tissue injury, with capillary and small vessels being much more susceptible than large vessels. Using the bubble dynamic Rayleigh–Plesset (R–P) equation to explain these phenomena, the results exhibit obvious differences between the theoretical calculations and experimental observations. The reason is that the R–P equation describes only the spherical motion mode where the bubble is in an unbounded fluid field [8]. While the constrained oscillation is characteristic of the dynamics of cavitation bubbles inside blood vessels,

* Corresponding author. Tel.: +86 27 87557843.
E-mail address: chxiong@mail.hust.edu.cn (C. Xiong).

1002-0071/$ - see front matter © 2009 National Natural Science Foundation of China and Chinese Academy of Sciences. Published by Elsevier Limited and Science in China Press. All rights reserved.
doi:10.1016/j.pnsc.2008.10.016

especially inside capillary and small blood vessels, further constraint effects of the vessel wall need to be taken into account. Church has mentioned that the vascular constraint should be considerable in his theoretical analysis [9], and Zhong et al. also discovered from experiments that the peak pressure exerted on the vessel due to the bubble oscillation is significantly larger than that predicted by the R–P equation [10]; unfortunately, acknowledging a proper model for the asymmetric interaction is still unavailable. In addition, the recent experimental observations further confirmed that the bubble shape will no longer remain spherical within the microvessel [11]. Therefore, there is an urgent need to perfect an appropriate theoretical model, to reveal the rule of the bubble coupled oscillation in ultrasound treatments, such as targeted drug delivery, as well as in the mechanism of microvascular damage.

Hu et al. have developed an ellipsoid evolution model for describing asymmetric oscillation of a bubble under the constraint of the microtube and analyzed the impact effects of the vessel wall exerted by the oscillation of the bubble in the cases of the rigid wall and thin flexible wall [12,13]. They found that a larger initial bubble/vessel radius ratio may significantly make the oscillating bubble produce a larger peak pressure acted on the inner vessel wall. Nevertheless, their efforts cannot fully reveal the dynamic characteristics of the microvessel, because blood vessels are highly complex in both nonlinear material properties and stress–strain relations [14,15]. To this end, Gao et al. have established a dynamic model of the three-phase coupled oscillation by using the pseudoelastic constitutive relations of real blood vessels [16]. They studied the interaction effects such as the vessel inertia action and material parameter changes [17], the dynamic stress distribution, and its variation tendency of the microvessel under different blood pressures and blood viscosities [18]. However, comparing with the spherical bubble motion in unbounded surroundings, the asymmetric oscillation characteristics of the constrained bubble need to be further clarified. Moreover, the prolate ellipsoid shape of the bubble evolution within the micro blood vessel simulated from theoretical analysis [13,17,18] is different from the oblate ellipsoid shape inside the rigid wall observed from experimental analysis [19,20]; outwardly, there seems to be an inconsistency between these two cases. It should be noted that under strongly nonlinear oscillation conditions, the various constraints of interface boundaries, both in geometric status and in the extent of wall compliances, can significantly affect the bubble oscillation features [19–24]. For this purpose, in this paper, the asymmetric oscillation characteristics of the bubble inside the microvessel subjected to the shock wave are investigated, as well as the reasons for the bubble surface deformation, resulting from a wide range of wall compliance, wall length, and fluid liquidity, are also discussed. The results give some useful insights into the understanding of the dynamic behavior of the bubble–boundary interaction in ultrasound-assisted therapy.

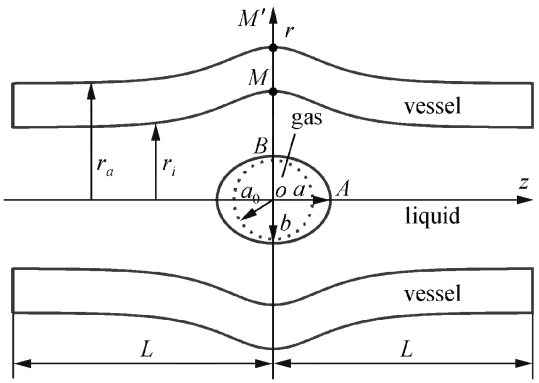

Fig. 1. A schematic illustration of the bubble–vessel-coupled oscillation system.

2. Problem description

The bubble motion inside a microvessel subjected to a shock wave can be considered a coupled model of the bubble–liquid–vessel oscillation system as shown in Fig. 1. In current cylindrical coordinates (r, θ, z), a gas bubble, initially spherical with radius a_0, suspends in liquid at the center of a circular vessel with initial inner radius r_i^0 and outer radius r_a^0. After the impact from a shock wave, the bubble contracts immediately into a revolving ellipsoid with the z-axis under the axisymmetric condition and exhibits nonspherical deformation characteristics. Synchronously, the deformations are also presented in the flexible blood vessel. In the deformational state, we designate a and b as radii of a deformed bubble in the axial and radial direction, respectively. The inner and outer radii are represented as r_i and r_a, and $2L$ is the calculation length of the blood vessel.

3. Fundamental equations of the coupled oscillation system

3.1. Equations of bubble motion

(a) Gas governing equations. The gas inside the bubble is assumed to obey the polytropic law [10,13],

$$p_g V^{\kappa} = p_{ge} V_e^{\kappa} \tag{1}$$

where polytropic index $\kappa = 1.40$, p_{ge} and p_g stand for the gas initial pressure and current pressure, V_e and V are the bubble initial volume and current volume, respectively.

(b) Fluid governing equations. The blood is modeled as incompressible liquid lacking body force. It should be noted that the volume change induced by the liquid compressibility at the physiological blood pressure level is almost negligible compared with the one caused by the dilation and contraction of the vessel. The mass conservation and the balance equations of linear momentum for viscous incompressible liquid lead to the following equations [25],

$$\nabla \cdot \mathbf{u} = 0 \tag{2}$$

$$\rho_0 \frac{\partial \mathbf{u}}{\partial t} + \rho_0 (\mathbf{u} \cdot \nabla)\mathbf{u} + \nabla p - \mu \nabla^2 \mathbf{u} = 0 \tag{3}$$

where t is the time variable; velocity vector $\mathbf{u} = (u_r, u_z)$, where u_r and u_z, respectively, denote the velocity components in the radial and axial direction; liquid mass density $\rho_0 = 1059\ \mathrm{kg\ m^{-3}}$ and dynamic viscous coefficient $\mu = 1.23 \times 10^{-3}$ Pa s; p is the liquid pressure and the initial pressure $p_0 = p_{SB} + p_0^*$, in which the initial blood pressure $p_{SB} = 115$ mm Hg (≈15 kPa) and $p_0^* = 101$ kPa is an atmosphere pressure [18].

(c) Boundary conditions on the bubble surface. For the interaction of any bubble–liquid interface with neglecting the gas viscosity and liquid compressibility, the pressure boundary condition on the bubble surface is as follows [18,26],

$$p + p(t) = p_g - \sigma\left(\frac{1}{\rho_1} + \frac{1}{\rho_2}\right) + \mu\left(\frac{\partial u_j}{\partial x_k} + \frac{\partial u_k}{\partial x_j}\right) n_j n_k \tag{4}$$

where $\mathbf{n} = (n_1, n_2, n_3)^{\mathrm{T}}$ stands for the unit normal vector whose positive direction is from the liquid to the gas, ρ_1 and ρ_2 denote the curvature radii of the bubble, and $\sigma = 56 \times 10^{-3}\ \mathrm{N\ m^{-1}}$ the surface tension coefficient. Ultrasound-induced pressure $p(t)$ is exerted on the bubble surface from an instant time $t = 0$ to $t = 1/2f$, i.e. [13]

$$p(t) = Ap_0^* e^{-\alpha t} \cos\left(2\pi f t + \frac{\pi}{3}\right), \quad 0 < t \le 1/2f \tag{5}$$

where the shock wave frequency $f = 100$ kHz, pressure amplitude coefficient $A = 25$, and delay parameter $\alpha = 3.5 \times 10^7$. Additionally, the bubble wall velocity $\mathbf{u}^{\mathbf{b}}$ should be equal to the liquid velocity $\mathbf{u}$ on the bubble surface, that is

$$\mathbf{u}^{\mathrm{b}} = \mathbf{u} \tag{6}$$

(d) Motion equations of the unconstrained bubble. Under the conjecture of spherical symmetry, the bubble remains in spherical motion in the unbounded fluid. In obtaining (1) and (4), we derive the pressure balance equation with the spherical symmetrical condition on the bubble surface,

$$p = p_g - \frac{2\sigma}{\rho_0} - 4\mu\frac{\dot{a}}{a} \tag{7}$$

Similarly, from the liquid governing equations and far-field conditions at infinity, we obtain

$$a\ddot{a} + \frac{3}{2}\dot{a}^2 + \frac{4\mu}{\rho_0 a}\dot{a} = \frac{1}{\rho_0}[p + p(t) - p_\infty] \tag{8}$$

Eq. (8) is the famous Rayleigh–Plesset bubble dynamic equation, in which a represents the bubble radius, $\dot{a}$ and $\ddot{a}$ respectively denote the velocity and acceleration on the surface of the spherical bubble, and the far-field pressure $p_\infty = p_0$. The analytical solutions of the Rayleigh–Plesset equation and various modified models match remarkably well with the practical results for the dynamics of cavitation in an unbounded field where the ambient fluid region is far larger than the bubble scale. While the constrained oscillation is characteristic of the dynamics of cavitation bubbles inside the blood vessel, especially inside the capillary and small blood vessel, further constraint effects of the vessel wall need to be taken into account.

3.2. Equations of the constraint vessel wall

(a) Constitutive relation of the vessel wall. Considering the pseudoelastic constitutive relation, a circular cross section of the vessel wall with inner radius r_i and outer radius r_a in current configuration (r, θ, z) will open up into a sector due to the effect of residual stress in referential configuration (R, Θ, Z) (zero stress state) [14,15], with R_i and R_a as the referential inner and outer radius, respectively. The relationships between the current state and the referential state are as follows,

$$r = r(R, Z, t), \quad \theta = (\pi/\Theta_0)\Theta, \quad z = \lambda\Lambda Z + D_z(R, Z, t) \tag{9}$$

where Θ_0 and Λ are the opening angle and axial stretch, respectively; λ is an additional load-induced axial stretch [16]. Moreover, the axial vessel displacement $D_z(R, Z, t)$ is derived from two parts: one is the axial deflection induced by blood vessel dilation/contraction and another is that caused by shear stress action from blood viscosity along the vessel wall [18].

Then, the deformation gradient tensor $\mathbf{F}$, Green strain tensor $\mathbf{E}$, and Cauchy stress tensor $\mathbf{t}$ are introduced

$$\mathbf{F} = (\partial(r, \theta, z)/\partial(R, \Theta, Z)) \tag{10}$$

$$\mathbf{E} = \mathbf{E}^{\mathrm{T}} = (\mathbf{F}^{\mathrm{T}} \cdot \mathbf{F} - \mathbf{I})/2 \tag{11}$$

$$\mathbf{t} = -P\mathbf{I} + \mathbf{F} \cdot (\partial W/\partial \mathbf{E}) \cdot \mathbf{F}^{\mathrm{T}} \tag{12}$$

in which $\mathbf{I}$ is the identity tensor, P is a Lagrange multiplier that enforces incompressibility, and W is a pseudoelastic strain-energy function, namely,

$$\begin{aligned} W &= \frac{1}{2}c(e^Q - 1) \\ Q &= c_1E_{RR}^2 + c_2E_{\Theta\Theta}^2 + c_3E_{ZZ}^2 + 2c_4E_{RR}E_{\Theta\Theta} + 2c_5E_{\Theta\Theta}E_{ZZ} \\ &\quad + 2c_6E_{ZZ}E_{RR} + c_7(E_{R\Theta}^2 + E_{\Theta R}^2) + c_8(E_{\Theta Z}^2 + E_{Z\Theta}^2) \\ &\quad + c_9(E_{RZ}^2 + E_{ZR}^2) \end{aligned} \tag{13}$$

where c is a material parameter having unit of stress, and c_i $(i = 1, 2, \ldots, 9)$ are non-dimensional material parameters.

To determine the geometric relation between the current configuration and the referential configuration, the incompressibility condition of the solid vessel wall is considered as follows:

$$\det\mathbf{F} = 1 \to \frac{\partial r}{\partial R} \cdot \frac{r\pi}{R\Theta_0} \cdot \frac{\partial z}{\partial Z} - \frac{\partial r}{\partial Z} \cdot \frac{r\pi}{R\Theta_0} \cdot \frac{\partial z}{\partial R} = 1 \tag{14}$$

(b) Equilibrium equations of the vessel wall. For the axially symmetric problem, $t_{r\theta} = t_{\theta z} = 0$, the equilibrium equations are

$$\frac{\partial t_{rr}}{\partial r}+\frac{\partial t_{zr}}{\partial z}+\frac{t_{rr}-t_{\theta\theta}}{r}=\rho\ddot{r}$$
$$\frac{\partial t_{zz}}{\partial z}+\frac{\partial t_{rz}}{\partial r}+\frac{t_{rz}}{r}=\rho\ddot{z} \tag{15}$$

where $\rho = 0.9 \times 10^3$ kg m^{-3} is the density of the vessel wall, and $\ddot{r}$ and $\ddot{z}$ denote the radial and axial acceleration, respectively [27],

$$\ddot{r}=[\mathrm{d}^2 r(R,Z,t)/\mathrm{d}t^2]\big|_{R,Z}$$
$$\ddot{z}=[\mathrm{d}^2 z(R,Z,t)/\mathrm{d}t^2]\big|_{R,Z} \tag{16}$$

(c) Boundary conditions of the vessel wall. On the interface of the internal wall, the normal stress should be equal to the liquid pressure p_i and the tangential stress equate the shear stress τ_i which is induced by the viscous fluid flow,

$$t_{zz}\sin^2\vartheta_i + t_{rr}\cos^2\vartheta_i - 2t_{rz}\sin\vartheta_i\cos\vartheta_i = -p_i$$
$$(t_{zz}-t_{rr})\sin\vartheta_i\cos\vartheta_i - t_{rz}(\cos^2\vartheta_i-\sin^2\vartheta_i)=\tau_i \tag{17}$$

where ϑ_i stands for the inclined angle between the positive normal of the inner vessel wall surface and the positive r direction.

In addition, the internal wall velocity $\mathbf{u}^{\mathrm{v}}$ should be equal to the liquid velocity $\mathbf{u}$ at the same point, i.e., no-slip condition,

$$\mathbf{u}^{\mathrm{v}}=\mathbf{u} \tag{18}$$

On the outer surface of the blood vessel, the ambient pressure p_a is assumed as an atmosphere pressure and absence of shear stress,

$$t_{zz}\sin^2\vartheta_a + t_{rr}\cos^2\vartheta_a - 2t_{rz}\sin\vartheta_a\cos\vartheta_a = -p_a$$
$$(t_{zz}-t_{rr})\sin\vartheta_a\cos\vartheta_a - t_{rz}(\cos^2\vartheta_a-\sin^2\vartheta_a)=0 \tag{19}$$

where ϑ_a stands for the inclined angle between the positive normal of the outer vessel wall surface and the positive r direction.

(d) Interface boundary conditions at two ends. For a real blood vessel in the closed circulatory system, two end boundaries at $z=\pm L$ should be in an infinite location so that both the liquid and the vessel remain in an undisturbed state during the oscillation of the bubble, herein, the boundary conditions are set as,

$$u_z=0, \quad \text{or} \quad p=p_0 \quad \text{for liquid},$$
$$D_z(R,Z,t)=0, \quad \text{for vessel}. \tag{20}$$

4. Results and discussion

4.1. Analysis model of the gas–liquid–vessel-coupled oscillation

Generally, the R–P equation is adopted to solve the problem of the bubble oscillation in the unbounded fluid field. When the interface conditions of the microvascular constraint are taken into account, numerical iterative methods are necessarily proposed in our analyses and calculations since the analytical methods become quite difficult for the nonlinear characteristics of the three-phase coupled oscillation between liquid and solid. The finite volume method is applied to compute the fields of velocity and pressure in liquid [25], and the finite difference technique is employed to calculate the stresses within the vessel wall. The liquid grids, vessel grids and the time step are set to be 3.14×10^{-2} μm × 3.14×10^{-2} μm, 3.14×10^{-2} μm × 5×10^{-2} μm and 4×10^{-4} μs, respectively. The discretion grids of the vessel wall are drawn in the current configuration for convenience, and the boundary grids should be matched with the liquid meshes for coupled boundary. At the beginning of our computation, we assume an interface pressure distribution $p_0(j)$ in advance, e.g., a constant pressure p_0 distribution, where j stands for the jth grip node on the liquid–vessel interface. Then, the velocities and pressures in the liquid field can be solved without involving the coupling with the vessel wall. Subsequently, using the obtained velocities and displacements of the liquid on the liquid–vessel interface as the boundary conditions of the vessel wall acted by the liquid, we can obtain the stress fields within the vessel wall and the corresponding boundary traction $p_1(j)$ on the interface. Following, we will use $p_1(j)$ instead of $p_0(j)$ as the interface pressure condition and conduct the same computation process as above to obtain $p_2(j)$ to $p_n(j)$ in turn. If the precision requirement $|p_n(j)-p_{n-1}(j)|/p_{n-1}(j) \leqslant 1 \times 10^{-3}$ has been satisfied, the computation at this time step will be regarded as convergent, and the computation can be moved into the next time step; otherwise, the iterative process continues until satisfying the convergence condition. In the iterative procedure, the results of variable values for each step are used as the initial values at the next time step.

In the initial state, the bubble radius is set as $a_0 = 5$ μm. For the vessel wall, the geometric parameters are set as inner radius $r_i^0 = 10$ μm and wall thickness $h_0 = 1$ μm, and the material parameters are chosen as [16],

$$c = 22.4 \text{ kPa}, \ c_1 = 0.0499, \ c_2 = 1.0672, \ c_3 = 0.4775,$$
$$c_4 = 0.0042, \ c_5 = 0.0903, \ c_6 = 0.0585, \ c_{7\text{–}9} = 0,$$
$$\Theta_0 = 71.4^\circ, \ \lambda = 1.8, \ \Lambda = 1.0177. \tag{21}$$

4.2. Asymmetric oscillation characteristics of a constrained bubble

To analyze the coupling oscillation system as shown in Fig. 1, consider that the microvessel is located in a closed circulatory system. Two cut-end boundaries at $z=\pm L$ should be at infinity so that both the liquid and the vessel remain in an undisturbed state during the oscillation of the bubble, i.e. $L \gg a_0$, we set the vessel half length $L = 100a_0$, $\mathbf{u} = 0$ for liquid and $r(t) = r(0)$ for the solid tube.

Fig. 2a shows the dependence of two principal axis radii upon time at Points A and B in the course of the bubble oscillation. The numerical results show that the onset of contract–expand periodic oscillations of the constrained bubble takes place immediately after the impact of the

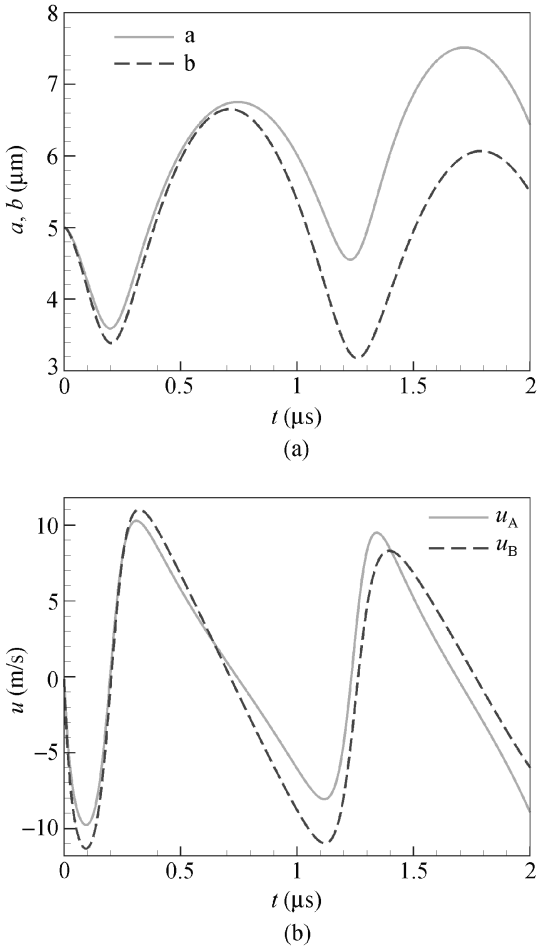

Fig. 2. (a) Dependence of the bubble radii upon time for the asymmetric oscillation and (b) dependence of the bubble velocities upon time for the asymmetric oscillation.

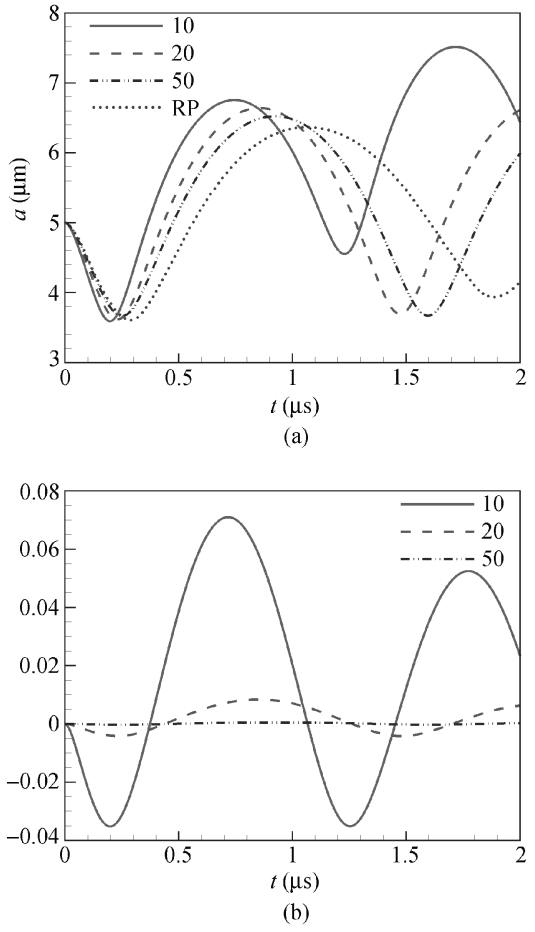

Fig. 3. (a) Bubble oscillation characteristics with various constraint vessels and (b) dependence of the vessel deformation rate upon time.

shock wave. On one hand, it appears as an obviously large deformation feature due to acute changes of the bubble radii. On the other hand, it exhibits nonspherical symmetric oscillation characteristics since the two principal axis radii are no longer equal in bubble motion, while the axial radius a is greater than the radial radius b. Fig. 2b describes the semi-axis velocities vs. time, in which u_A denotes the velocity for Point A and u_B for Point B. In this figure, we find that the change in the amplitude of u_A is greater than that of u_B as the bubble oscillates; the circumferential motion is more violent than axial. Evidently, the constraint effects of the vessel wall lead to the asymmetrical phenomenon of the bubble oscillation.

For further investigation on the vessel wall constraint, we maintain the same shock wave strength and fix the bubble initial radius a_0, and set the inner vessel radii $r_i^0 = 10,\ 20,\ 50$ μm to analyze the bubble oscillation regularity with various constrained vessels as well as the unbounded fluid (R–P equation). In Fig. 3a, when the vessel radius decreases gradually from infinity (unbounded field) to $r_i^0 = 10$ μm, we observe that the smaller radius of the vessel results in more severe oscillation of the bubble with larger amplitude, shorter period, and higher frequency.

Considering the coupled effects synchronously, the vessel deformation is also induced by the bubble oscillation. We let $e = (r_i - r_i^0)/r_i^0$ represent the deformation degree of the blood vessel and analyze the maximum deformation at Point M ($r = r_i$, $z = 0$) along the inner wall in each time step. Fig. 3b shows that the synchronized deformations of the vessel wall are induced by the bubble oscillation, i.e., the vessel contracts with the decrease in the bubble size, and vice versa. We also find in this figure that when the wall radius increases, the corresponding deformation becomes gradually weakened and the coupling effect is reduced, which further indicates that the free oscillation rule of a spherical bubble is still applied in the bubble oscillation when the wall geometric dimension is much larger than the bubble. That is, the asymmetric phenomenon of the bubble oscillation exists in the microvessel, but for the constraint condition of the farther boundary, does not appear within a large blood vessel; thus, the bubble oscillations consistently satisfy the R–P equation.

To analyze the bubble asymmetry for convenience, we define the ellipticity $\varepsilon = (a - b)/a$ to characterize the asymmetrical measure and plot the bubble ellipticity vs. time both for various vessel radii shown in Fig. 4a and for various ultrasound pressures shown in Fig. 4b. It is observed from Fig. 4a that asymmetrical measure seems to appear less while the r_i^0 is 10-fold of the a_0, but with the vessel radius stepping down, asymmetrical measure becomes visible, especially when $r_i^0 = 10$ μm, it appears that there is significant asymmetric oscillation. The reason for this phenomenon is derived from the constraint action of the vessel wall when the bubble magnitude approaches the vessel radius. In addition, considering the strength of the shock wave is also an important factor for the bubble oscillation, we keep the same material parameters in Fig. 4a and fix the initial bubble radius $a_0 = 5$ μm and vessel inner radius $r_i^0 = 10$ μm, set the shock wave pressure amplitude $A = 15, 25, 35$ to analyze the asymmetric effects of the bubble oscillation. As shown in Fig. 4b, the peaks of the asymmetrical measure ε magnify with the increasing pressure exerted on the bubble surface, which means that the higher the energy imposed, the more violent the asymmetric oscillation becomes. Therefore, the pressure amplitude of the shock wave is the most direct factor; while it goes up to a critical threshold, the bubble rupture may take place.

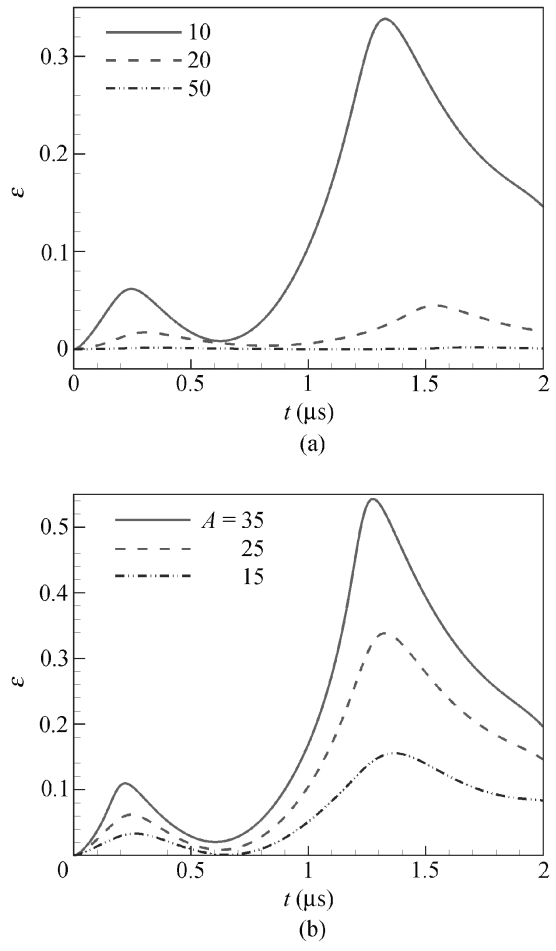

Fig. 4. Dependence of the bubble ellipticity upon time: (a) for various vessel radii and (b) for various pressure amplitudes.

It is also found from Figs. 4a and b that the bubble flat degree in the circumferential direction is always larger than that in the axial direction, resulting in the prolate ellipsoid profile $a > b$ throughout the course of the bubble oscillation, which will be discussed in the following. We have observed from Fig. 2b that the change in the amplitude of u_B is higher than that of u_A in the first period during the bubble motion; thus, the circumferential radius b decreases faster than the axial radius a, which consequently leads to the asymmetrical measure ε elevating at the bubble contraction stage, and vice versa, ε decreasing at the bubble expand stage. Moreover, we can observe an interesting result that the second peak of the asymmetrical measure is larger than the first peak. The main reason for this phenomenon is the different initial conditions: in Fig. 4, during each oscillation period (time T), the bubble ellipticity increases at the bubble contraction stage and reaches the peaks at time $t = T/4$ and $t = 5T/4$. As we all know, the initial condition is the dominant factor in determining the early motion features. When the bubble begins to shrink at $t = 0$, the whole system including the bubble, fluid, and vessel wall is still in static status, and the bubble surface is forced by an instant-pulse ultrasonic pressure. Conversely, for the second contraction stage, the coupled system is in motion state with certain velocity and acceleration at $t = T$. Owing to the viscous damping, of course, after the second circle, the oscillation amplitudes are gradually attenuated with the time elapsing.

As can be seen via the above analyses, the geometric constraint of the vessel wall is one of the dominant factors for the bubble asymmetric oscillation, which is significantly different from the free flow field. With the tube radius decreasing, the bubble oscillation appears to possess some behaviors such as shorter cycle and higher frequency, which is coincident with the calculated result under the deformable wall constrained [24], but is different to the results of the theoretical calculation and experimental observation under the rigid wall constrained [19,22]. It is therefore necessary to further delve into the interface boundary effects on the bubble oscillation characteristics.

4.3. Effects of interface boundaries on bubble shape evolution

In incompressible liquid, the volume change owing to the bubble motion must be entirely compensated by the fluid flow; thus, the tendency of the bubble shape variety should be determined by the change in the direction of flow. In the meantime, the vibration mode of the bubble constrained in the microvessel is saliently influenced not only by the factors such as the initial conditions of configuration and vessel compliance, but also by those factors associated with the two far-end boundary conditions at $z = \pm L$, which is completely different from the free oscillation mode in the unbounded field. It can be said that the inlet/outlet boundary conditions at far cut ends

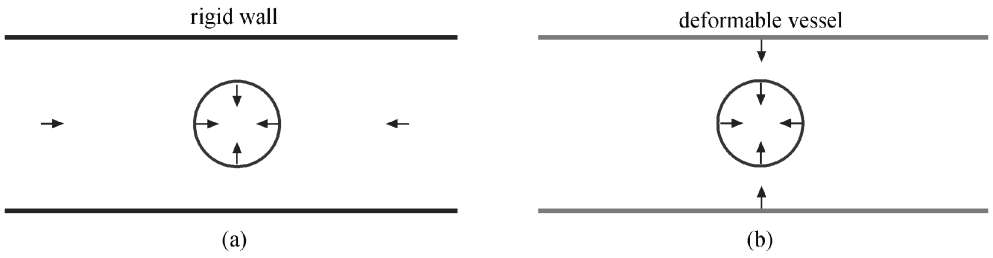

Fig. 5. A schematic illustration of the fluid volume compensation: (a) axial dominance and (b) radial dominance.

($z = \pm L$), to a certain extent, may be the dominant factor that can decide which mode for the bubble is evolving. To determine which kind of shrink direction of the elliptic bubble will present during the asymmetric oscillation, i.e., $a > b$ or $b > a$, in this section, we discuss the change of the bubble profile features during the asymmetric oscillation. As an example, we analyze the contraction process of the bubble from $t = 0$ to the time of minimizing volume in detail. Similar to this analysis, the bubble expanding behavior will not be discussed any longer in the present paper.

For a constraint wall with conventional materials, the vessel deformation induced by the bubble oscillation is far less than the bubble deformation in the order of magnitude so that the vessel volume change is almost negligible and the tube can be regarded as a rigid vessel [28]. Therefore, the bubble volume change should be nearly compensated by liquid flowing in the axial direction (see in Fig. 5a). We note that a bubble will not be able to oscillate in incompressible liquid existing inside a rigid vessel with infinite length, because it will need infinite energy to accelerate the static liquid. Thus, if the bubble is inside a rigid vessel filled with incompressible liquid, the vessel length must be set finite and the liquid velocity u_z on the boundary $z = \pm L$ must not vanish; otherwise, no bubble oscillation happens, i.e., in this case, the coupling system is an opening state in which the volume change of the bubble contraction can be compensated by the fluid inflowing through the two cut ends.

In our vascular model, the microvessel locates in the closed circulatory system, and the length is far larger than its radius; thus, the boundary condition of two cut ends is set as $u_z = 0$ at $z = \pm L$. In addition, like many soft tissue materials, the blood vessel is facilely deformed with fluctuating blood pressure (e.g. pulse) since its rigid coefficient is far less than the common tube. For this kind of large compliance vessel without liquid flow at far cut ends, the entire volume changes of the bubble motion are totally compensated by the shrink deflection of the vessel. As a result, the liquid movement is dominant in radial velocities, as seen in Fig 5b.

To analyze the bubble profile in various boundary conditions of interface constraint, we select three representative boundary conditions, which are the rigid constrained boundary of a rigid vessel wall in finite length, the flexible constrained boundary of a blood vessel in infinity, and the infinite boundary in the unbounded flow field. Firstly, for a rigid microvessel, we set the circumferential stiffness coefficient $c_2^F = 30c_2$ to simulate the rigid vessel constraint, and let $L^F = 10a_0$ to satisfy both the finite length condition of the vessel wall, and minimize the disturbing effects induced by the movement of two cut ends in the coupled vibration system. The boundary condition of the cut ends is set as $p + \rho u_z^2/2 = p_0|_{z=\pm L}$, that is, allowing the fluid inflow/outflow. Numerical results reveal the varieties of the bubble upon time, as shown in Fig. 6a; during the bubble contraction stage, the axial radius is significantly higher than the radial radius due to the majority fluid flow in the axial direction, i.e., oblate ellipsoid surface $b > a$, which are all in reasonable agreement with the results of related theoretical prediction and experimental observation [19–21]. Secondly, for a vascular system mentioned in the above section, we let wall length $L = 100a_0$ and $u_z = 0$ as the boundary condition at two ends. The bubble shape changes can be seen in Fig. 6b, where the bubble constriction in the z-axis shrinks faster than the r-direction, resulting in $a > b$ on its prolate elliptic surface, which are consonant with the analytic solution by adopting the deformable microvessel model [13,23]. Finally, for infinite boundary without the vessel constrained, we also plot Fig. 6c for the convenience of comparison, to manifest the contraction process of the

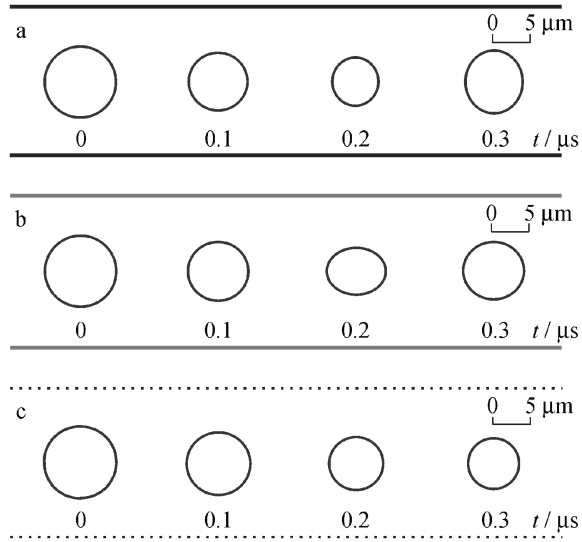

Fig. 6. Effects of the bubble profile within different interface boundary conditions: (a) rigid constrained boundary, (b) vascular constrained boundary and (c) unbounded boundary.

bubble oscillating in the free flow field. Thus, it can be found that some special features of biological tissue materials and peculiar characters of oscillation evolution during the bubble motion inside the microvessel are induced by the shock wave, which need more perfect models in theoretical analysis and advanced technological means in experimental validation, and will be taken into consideration for further research.

5. Conclusions

We develop a three-phase coupled model of the gas–liquid–solid oscillation system to analyze the profile changes of a bubble inside a micro blood vessel subjected to a shock wave and the corresponding bubble dynamic characteristics. The numerical results reveal that in a closed circulatory system, the asymmetric scale of the bubble and the coupled effect of the vessel seem little appearance when the vessel size is far larger than the bubble measure; but as the vessel radius reduces gradually and approaches the bubble radius with the same order, it appears that there are significant asymmetric effects in the confined bubble and this causes large coupled deformation in the vessel wall. Throughout the course of the oscillation, the bubble is mainly flat along with the radial direction, and maintains its elliptic shape of that the axial radius is larger than radial radius, i.e., $a > b$. The reason for these phenomena is that the profile changes of a bubble motion are determined by the compensation mode of the liquid volume: For an infinite vascular system, the volume-compensated way is entirely derived from the deformable compliance vessel. This is an extraordinary phenomenon which only appeared in the microvascular system. On the contrary, for an opening finite vessel system, the volume compensation induced by the bubble contraction mostly comes from the inflow liquid at the ends, so that the axial contraction is larger than the radial and exhibits another phrase of the bubble shape varieties, i.e., the bubble is mainly flatted along with the radial direction which is consistent with the results of theoretical analysis and experimental observation. The conclusions not only give a reasonable explanation for the difference and connection of the bubble shape changes with the asymmetrical oscillation in existing literatures, but also reveal some unique attributes of the bubble oscillation within the microvascular system, which provides even more insights into the bubble-vessel-coupled dynamics. In physical mechanism, the bubble oscillation inside the micro blood vessel plays a dominant role in ultrasound treatments in vivo, and many issues such as the bubble ruptures and vascular injuries need to be further studied in future.

Acknowledgements

This work was supported by the China Postdoctoral Science Foundation (Grant No. 20070420906), the National Natural Science Foundation of China (Grant No. 50775080), the Hi-Tech Research and Development Program (863) of China (Grant No. 2007AA04Z204), and the National Key Technology R&D Program of China (Grant No. 2008BAI50B04).

References

[1] Klibanov AL. Microbubble contrast agents: targeted ultrasound imaging and ultrasound-assisted drug-delivery applications. Invest Radiol 2006;41(3):354–62.
[2] Ferrara K, Pollard R, Bordeni M. Ultrasound microbubble contrast agents: fundamentals and application to gene and drug delivery. Annu Rev Biomed Eng 2007;9:415–47.
[3] Bloch SH, Short RE, Ferrara KW, et al. The effect of size on the acoustic response of polymer-shelled contrast agents. Ultrasound Med Biol 2005;31(3):439–44.
[4] Wells PNT. Ultrasound imaging. Phys Med Biol 2006;51:R83–98.
[5] Gao FR, Hu HP, Hu YT. Effects of an outer layer and its damping on acoustic scattering characteristics of a double-layered spherical shell immersed in water. J Huazhong Univ Sci Technol 2004;32(6):102–4.
[6] Rapoport N. Stabilization and activation of pluronic micelles for tumor-targeted drug delivery. Colloid Surf B Biointerfaces 1999;16(1–4):93–111.
[7] Paliwal S. Ultrasound-induced cavitation: applications in drug and gene delivery. Expert Opin Drug Deliv 2006;3(6):713–26.
[8] Feng ZC, Leal LG. Nonlinear bubble dynamics. Annu Rev Fluid Mech 1997;29:201–43.
[9] Church CC. A theoretical study of cavitation generated by an extracorporeal shock wave lithotripter. J Acoust Soc Am 1989;86(1):215–27.
[10] Zhong P, Zhou YF, Zhu SL. Dynamics of bubble oscillation in constrained media and mechanisms of vessel rupture in SWL. Ultrasound Med Biol 2001;27(1):119–34.
[11] Zhao SK, Ferrara KW, Dayton PA. Asymmetric oscillation of adherent targeted ultrasound contrast agents. Appl Phys Lett 2005;87(13):134103.
[12] Hu YT, Qin SP, Hu T, et al. Asymmetric oscillation of cavitation bubbles in a microvessel and its implications upon mechanisms of clinical vessel injury in shock-wave lithotripsy. Int J Nonlinear Mech 2005;40(2–3):341–50.
[13] Qin SP, Hu YT, Jiang Q. Oscillatory interaction between bubbles and confining microvessels and its implications on clinical vascular injuries of shock-wave lithotripsy. IEEE Trans Ultrason Ferroelectr Freq Control 2006;53(7):1322–9.
[14] Chuong CJ, Fung YC. Three-dimensional stress distribution in arteries. ASME J Biomech Eng 1983;105(3):268–74.
[15] Chuong CJ, Fung YC. On residual stresses in arteries. ASME J Biomech Eng 1986;108(2):189–92.
[16] Humphrey JD, Na S. Elastodynamics and arterial wall stress. Ann Biomed Eng 2002;30(4):509–23.
[17] Gao FR, Hu YT, Hu HP. Asymmetrical oscillation of a bubble confined inside a micro pseudoelastic blood vessel and the corresponding vessel wall stresses. Int J Solids Struct 2007;44(22–23):7197–212.
[18] Hu YT, Gao FR, Hu HP, et al. Interactions inside a coupled oscillation system of bubble–viscous liquid–vessel and the induced stresses and strains within the vessel wall. J Mech 2008;24(1):55–61.
[19] Tomita Y, Robinson PB, Tong RP, et al. Growth and collapse of cavitation bubbles near a curved rigid boundary. J Fluid Mech 2002;466:259–83.
[20] Tomita Y, Kodama T. Interaction of laser-induced cavitation bubbles with composite surfaces. J Appl Phys 2003;94:2809–16.

[21] Shima A, Sato Y. The behavior of a bubble between narrow parallel plates. J Appl Math Phys (ZAMP) 1980;31:691–704.
[22] Sassaroli E, Hynynen K. Resonance frequency of microbubbles in small blood vessels: a numerical study. Phys Med Biol 2005;50(22):5293–305.
[23] Qin SP, Ferrara KW. Acoustic response of compliable microvessels containing ultrasound contrast agents. Phys Med Biol 2006;51(20):5065–88.
[24] Qin SP, Ferrara KW. The natural frequency of nonlinear oscillation of ultrasound contrast agents in microvessels. Ultrasound Med Biol 2007;33(7):1140–8.
[25] Ferziger JH, Peric M. Computational methods for fluid dynamics. New York: Springer Verlag; 2001.
[26] Landau LD, Lifshits EM. Continuum mechanics. Moscow: Gostekhizdat; 1954.
[27] Humphrey JD. Cardiovascular solid mechanics: cells, tissues, and organs. New York: Springer Verlag; 2002.
[28] Ye T, Bull JL. Direct numerical simulations of micro-bubble expansion in gas embolotherapy. ASME J Biomech Eng 2004;126(6):745–59.